Article

V-Band Channel Modeling, Throughput Measurements, and Coverage Prediction for Indoor Residential Environments

Brecht De Beelde [1,*,†] , **Andrés Almarcha** [1,2] , **David Plets** [1] and **Wout Joseph** [1]

1   Department of Information Technology, Ghent University/IMEC, 9052 Ghent, Belgium;
    Andres.Almarcha@gmail.com (A.A.); David.Plets@UGent.be (D.P.); Wout.Joseph@UGent.be (W.J.)
2   Barcelona Supercomputing Center, 08034 Barcelona, Spain
*   Correspondence: Brecht.DeBeelde@UGent.be
†   Current address: Technologiepark-Zwijnaarde 126, 9052 Ghent, Belgium.

Abstract: With the increased resolution and frame rates of video recordings, in combination with the current evolution towards video-on-demand streaming services and the user expecting ubiquitous wireless connectivity, it is necessary to design wireless communication systems that allow high-rate data transfer. The large bandwidths that are available in the mmWave frequency band allow such high data rates. In this paper, we provide an experimental and simulated indoor residential radio channel model at V-band frequencies and perform packet error rate and throughput measurements at 60 GHz using IEEE 802.11ad transceivers. We compare the path loss and throughput measurements to simulations using a network performance prediction tool. The path loss measurement results using an omnidirectional transmit antenna correspond well to generic indoor mmWave channel models. Double-directional path loss measurements show that generic models underestimate path loss of non-Line-of-Sight (NLOS) links. A ray-launching algorithm is designed and validated, and used for IEEE 802.11ad throughput estimation based on link budget calculations. The link budget underestimates the achieved throughput, when comparing to adaptive-rate MCS selection in a commercial transceiver, based on the measured signal-to-noise ratio. Packet error rate measurements confirm that, even for NLOS links, throughputs exceeding 1 Gbps are possible.

Keywords: mmWave; V-band; channel modeling; path loss; throughput measurements; network performance; residential; indoor

1. Introduction

Wireless connectivity has become essential in our daily lives, and as the amount of internet traffic exponentially increases, e.g., due to high-definition and high-framerate video streaming, there is a need for high-throughput wireless communication systems. At mmWave frequencies, large bandwidths are available that enable establishing such high-capacity wireless links. In the last decade, transceivers and standards have been developed for communication using a 60 GHz carrier [1,2], but the characterization of the mmWave radio channel for both indoor and outdoor environments is still ongoing.

Cellular connectivity at mmWave frequencies is introduced in fifth-generation (5G) wireless communication, and the 60 GHz industrial, scientific, and medical (ISM) band is targeted for wireless fiber technology in which high-throughput wireless communication technologies replace wired access networks. Standardization activities took place for the design of wireless technologies in the mmWave frequency bands, resulting in the IEEE 802.11ad standard for high-throughput wireless communication using 2 GHz channels and a center frequency of 60 GHz [1], and its successor IEEE 802.11ay [2,3] that introduces channel bonding and supports up to four multiple-input multiple-output (MIMO) streams, amongst others. The international telecommunication union (ITU) has a recommendation on wireless systems using the 60 GHz frequency band [4].

1.1. Background and Related Work

1.1.1. Channel Models

Channel modeling for fixed wireless access applications is discussed in [5–7], and the third generation partnership project (3GPP) released a channel model for mmWave frequencies [8]. Outdoor radio channel measurements at mmWave frequencies are presented in [5], noting the sparsity of the outdoor radio channel. Building penetration loss measurements for fixed wireless access applications are presented in [6], with reported losses ranging from 9 dB to 17 dB. In [7], the authors performed outdoor measurements at 32 GHz and compared the measurement results to channel simulations.

Channel models at mmWave frequencies for indoor environments are presented in [9–20]. An overview of research on indoor propagation at mmWave and sub-THz frequencies, including a living room scenario, is presented in [9]. Only a Line-of-Sight (LOS) link is considered, and a single reflection is measured. 60 GHz channel models for a public shopping mall and office environments are discussed in [10–12] presents the 60 GHz channel model for a ship hull. Path loss differences between mmWave and sub-6 GHz bands are limited, whereas delay and angular spread differ significantly [10]. Path loss (PL) and delay spread of the 60 GHz radio channel of a hospital environment are presented in [13], and are found to be lower than for other indoor environments such as an office room. The indoor radio channel for large office and laboratory environments is characterized in [14], reporting few multipath components at 60 GHz. The directional characterization of the 60 GHz office channel is discussed in [15,16], concluding that scattering from smaller objects, including desktop displays, is characterized by specular reflections, and that channel clusters correspond to first-order and second-order reflections. Compared to indoor LOS channels, there is a larger variability in non-Line-of-Sight (NLOS) mmWave channel models [21]. PL exponent values for NLOS channel models for an office environment range from 2.7 to 5.4 [22,23]. Angular characteristics of the mmWave channel in the azimuth plane are found to be more dependent on antenna position and the environment, whereas in the elevation plane, they depend on the height difference [24]. Passive reflectors can be used to enhance coverage for NLOS links [25–27]. A statistical channel model for a conference room is provided in [17], i.e., blockage probabilities are assigned to channel clusters. In [28], the spatio-temporal channel model at 60 GHz is compared to the characteristics of the 70 GHz channel model. Spatio-temporal characteristics at the two frequencies are similar and reveal only weak diffuse scattering. Spatial and temporal characteristics of the 60 GHz indoor radio channel are provided in [18,19], confirming that only first-order and second-order reflections form relevant multipath components. In [29], the angular spread is simulated based on the 3GPP standard for different antenna types, and 6 GHz results are compared to 60 GHz, showing that directional antennas significantly reduce the angular dispersion. In [20], an indoor radio channel model for an office environment at 73 GHz is provided, and the indoor radio channel for an office environment at 140 GHz is characterized in [30–32]. In [33–35], the influence of human activity on an indoor 60 GHz wireless link is investigated, reporting an attenuation exceeding 20 dB when a body blocks the communication path. Estimation of walking speed using Doppler shift of a 60 GHz indoor signal is presented in [36]. In [37], it is shown that furniture in a residential environment greatly impacts the channel.

Indoor MIMO channel measurements in a lab at frequencies up to 30 GHz are presented in [38], concluding that the size of the antenna array influences the number of multipath components that are captured. Simulations and measurements in an office room for frequencies up to 30 GHz are presented in [39], and the indoor radio channel of a corridor and stairwell is characterized in [40] at 38 GHz. In [39], the authors draw the same conclusion as in [37], i.e., room furniture impacts the multipath characteristics of the channel. The indoor industrial channel at 28 GHz is characterized in [41], where a mean root-mean-square (RMS) angular spread value of 36° is reported for LOS scenarios, and 63.6° for NLOS.

1.1.2. Network Performance Simulations

Different methods exist for obtaining channel information and estimating network performance. A ray-tracer defines propagation paths between two antennas using a geometric approach, i.e., reflections and transmissions are defined, and losses are calculated via Fresnel coefficients. A ray-launcher uses a fixed transmit antenna location, and launches rays in the azimuth and elevation field, defining interactions with the environment using electric properties of the materials. Both methods work well if we have an accurate description of the environment, i.e., both the object dimensions as well as the electrical properties are known. If such information is not known, we can use generic channel models or use statistical ray-tracing methods. In this approach, scattering objects are positioned randomly, and the number of clusters depends on statistical channel parameters, including angular spread and diffuse scattering.

In [5], outdoor channel measurements are compared to the outcomes of a proprietary ray-tracer. The main drawback of this ray-tracer is that it relies on highly accurate light detection and ranging (LiDAR) point cloud data, and gathering such data is expensive. Statistical ray-tracing methods allow channel simulations when an accurate environmental layout is not available. In [7], it is found that QuaDRiGa, originally developed for sub-6 GHz systems, works well at 32 GHz and allows network performance evaluation for generic environments, based on statistical channel parameters such as the angular spread. Link budget estimation via ray-tracing for mmWave communication in outdoor environments is discussed in [42], but results are limited to a very simple environmental layout, with both antennas sandwiched between two parallel walls. In [43,44], the indoor coverage of 5G mmWave networks is discussed using system-level simulations, and a radio resource mapping scheme is proposed.

1.1.3. IEEE 802.11ad Network Performance, Transceivers and Radios

System-level simulations for wireless fiber using IEEE 802.11ad are presented in [45], A receiver design for an IEEE 802.11ad radio is presented in [46], and a configurable transmitter architecture is presented in [47]. A fully integrated transceiver chipset is presented in [48]. In [49], the authors investigate the performance of different modulation and coding schemes (MCS) in a Gaussian noise and multipath fading channel, concluding that the single-carrier modes (MCS 1 to 12) outperform the orthogonal frequency division multiplex (OFDM) modes in most cases. The performance of the IEEE 802.11ad medium access control (MAC) layer is discussed in [50]. Throughput measurements are presented in [51,52], and transmission control protocol (TCP) performance in an office room is discussed in [53]. In [54], a channel sounder is presented for mmWave radio channel modeling and IEEE 802.11ad system validation, which is being used by different research institutions [5,12,55–60].

1.2. Contributions

mmWave channel models do not exist for a residential environment, which differs significantly from other indoor environments such as an office room. However, high-throughput communication in residential environments is the main use case for mmWave wireless communication using the IEEE 802.11ad standard. In this paper, we performed indoor radio channel measurements in a living room environment, at frequencies ranging from 50 to 75 GHz, using a spectrum analyzer-based channel sounder. We also compared them to double-directional PL measurements using the Terragraph (TG) platform. Next to providing a residential channel model, it is the first time that network performance, i.e., packet error rate (PER) and throughput, is analyzed via measurements and channel model-based simulations. The channel model is implemented in a network coverage prediction algorithm that estimates received power and throughput for every location in an indoor environment, using a ray-launching algorithm. The network performance simulations combine environmental layout information with stochastic channel models. Therefore, coverage prediction for a specific environment is possible, and it will be shown that no cm-level accuracy of the environment model is required.

The outline of this paper is as follows. In Section 2, we first present the measurement equipment that we used for the channel measurement campaign and system-level measurements, followed by a description of the measurement setup. We present the prediction tool that we designed to analyze network performance of mmWave wireless systems for indoor environments in Section 3, In Section 4, we provide the angular PL measurement results and link the results to the PER and throughput measurements. We then compare the results to simulations using the coverage prediction tool. Section 5 concludes this paper.

2. Measurement Methodology

2.1. Measurement Equipment

2.1.1. V-Band Channel Sounder

The architecture of the channel sounder is presented in Figure 1. We use a signal generator type R&S SMB100A and spectrum analyzer type R&S FSVR40 to perform angular PL measurements. The signal generator generates a radio frequency (RF) source in the frequency range 8.3 GHz to 12.5 GHz, which is up-converted to the V-band via a frequency multiplier type R&S SMZ75 with multiplication factor 6. The signal is transmitted with 5 dBm output power using an omnidirectional antenna type Mi-Wave 267V/385 with a gain of 3 dBi and gain variations of 2 dB over the complete band. The transmit (TX) antenna has an elevation half-power beamwidth (HPBW) of 45° and is connected via a WR-15 rectangular waveguide. The signal is captured by a directional horn antenna type Steatite QSH-SL-50-75-V-20 with a gain of 20 dBi, and down-converted to an intermediate frequency (IF) in the range 5 MHz to 2 GHz, using a harmonic mixer type R&S FS-Z75. The receiving (RX) antenna has an HPBW of 18° at 60 GHz in both the elevation and azimuth plane. The harmonic mixer has a conversion loss of 18 dB and uses a local oscillator in the frequency range 8.0 GHz to 12.8 GHz which is provided by a spectrum analyzer that displays the received power. The analyzer's displayed average noise level (DANL) is −174 dBm/Hz and the noise figure at the IF port is 3 dB. The mixer's conversion loss is taken into account by the spectrum analyzer, and the cable losses and noise figure of the equipment are calibrated out. Therefore, the error margin is mainly defined by the gain variations of the antennas.
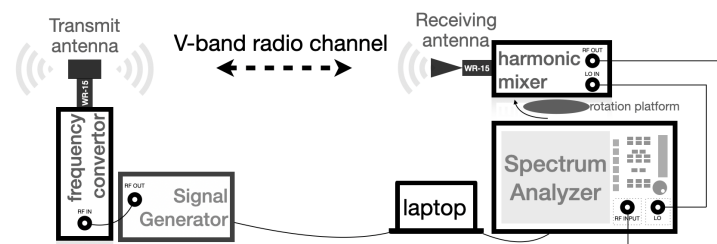

Figure 1. V-band channel sounding architecture.

A frequency sweep with a continuous wave signal is executed, with a frequency ranging from 50 to 75 GHz, in steps of 500 MHz. For each frequency, we perform a power measurement with the spectrum analyzer, using 501 frequency points, a span of 5 MHz, and an averaging factor of 4. We perform an angular scan, i.e., the receiving antenna is rotated in steps of 12°, which corresponds to the antenna's HPBW at the upper frequency. For every angle, we convert the measured received power P_{RX} in dBm to directional PL in dB via (1), with P_{TX} the transmit power in dBm, G_{TX} the antenna gain of the TX antenna in dBi, and G_{RX} the antenna gain of the RX antenna in dBi.

$$PL = P_{TX} + G_{TX} + G_{RX} - P_{RX} \tag{1}$$

Omnidirectional PL is calculated by interpolating the directional received power to an angle step-size equal to the antennas' HPBW, and summation of interpolated linear power values. With a TX power of 5 dBm, a total antenna gain of 23 dBi, a DANL of −151 dBm

using a resolution bandwidth of 100 Hz, a noise figure of 3 dB, a minimum signal-to-noise ratio (SNR) of 8 dB, and a conversion loss of 18 dB, the maximum measurable PL is 150 dB.

Based on the angular PL measurements, we calculate the mean angle of arrival AoA_{avg} via (2) and root-mean-square (RMS) angular spread AoA_{RMS} via (3), with $P_{RX}(\theta)$ the received power at an angle θ in degrees.

$$\text{AoA}_{\text{avg}} = \frac{\sum_{\theta} P_{RX}(\theta) \cdot \theta}{\sum_{\theta} P_{RX}(\theta)} \tag{2}$$

$$\text{AoA}_{\text{RMS}} = \sqrt{\frac{\sum_{\theta} P_{RX}(\theta) \cdot \theta^2}{\sum_{\theta} P_{RX}(\theta)} - \left(\text{AoA}_{\text{avg}}\right)^2} \tag{3}$$

2.1.2. Terragraph Platform

Next to power measurements using the channel sounder presented in Section 2.1.1, we also use the TG sounder platform presented in [54] to perform PL, PER, and throughput measurements. The TG platform consists of a pair of customized IEEE 802.11ad nodes each having an antenna array of 36 by 8 elements with an interspacing of 0.55 λ and the possibility for beamsteering via a phase shifter. When using all antenna elements, the antennas' HPBW is 2.8°. The azimuthal scanning range is $-45°$ to $45°$ in steps of 1.4°.

The nodes transmit and receive IEEE 802.11ad waveforms at RF channel identifier 2, with a center frequency of 60.48 GHz and a channel bandwidth of 2.16 GHz. At the transmitting node, we calculate the effective isotropically radiated power (EIRP) by combining antenna gain (which depends on the beam configuration) and power settings. The EIRP in our PL, throughput, and PER measurements is 32.8 dBm. The transceiver chipset of the receiving node reports received signal strength information (RSSI) which is combined with the receiver gain settings to obtain received power. The receiver sensitivity is -81 dBm. The nodes are calibrated and can be used to measure PL, by subtracting the received power from the EIRP and taking into account the RF and IF gain. Prior to the measurement campaign, the TG platform is validated in an anechoic room for a distance of 2 m between the nodes, as can be seen in Figure 2.

(**a**)   (**b**)
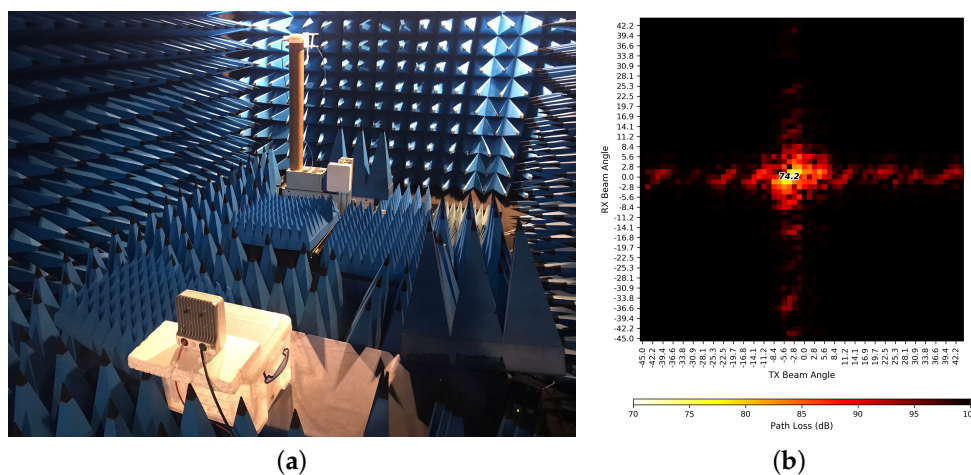
Figure 2. IEEE 802.11ad Terragraph platform validation in anechoic room, with a distance of 2 m between the antennas. (**a**) Measurement setup; (**b**) Angular path loss profile.

The measured PL is 74.22 dB which differs less than 1 dB from the free space PL (FSPL) of 74.09 dB, but sidelobes are present in the antenna radiation pattern, which results in a cross pattern when visualizing PL as a function of angle of departure (AoD) and angle of arrival (AoA).

In addition to PL measurements, we also use the TG platform for PER and throughput measurements. Prior to these measurements, a scan is performed over all TX-RX beam

combinations, and the beam combination for which the maximum SNR is obtained, is selected. The MCS index can be set from 1 to 12, all using a single-carrier physical (PHY) layer. The PER is measured by sending packets using the best beam combination, for all MCS indices and counting the number of packets that are correctly received. For the throughput measurements, frames are continuously sent using the best beam combination, and throughput is estimated based on the MCS that the IEEE 802.11ad transceiver would select in a real deployment. The adaptive rate mechanism of IEEE 802.11ad is not standardized, and the MCS selection is done in the transceiver's baseband, based on the channel information, mainly SNR, embedded with the data frames. The resulting throughput estimation provides an upper bound, based on the MCS index. Actual throughputs can be lower, due to packet loss.

2.2. Measurement Setup

Measurements are performed in an indoor residential environment, i.e., a living room with an area of 40 m^2, shown in Figure 3. We compare results of a LOS link with a distance of 4.7 m between the two antennas, to results of two NLOS links. The distance between the two antennas is 4.7 m for link NLOS1, and 3.4 m for link NLOS2. For both links, a wall obstructs the direct path, and communication is established through a reflecting path.

The goal of the measurements is to determine the link quality of a high-throughput wireless link for residential scenarios, such as high-throughput video streaming of high-resolution video and virtual reality. In realistic scenarios, the access point will be mounted close to the ceiling to decrease the number of obstacles in a cluttered environment. Therefore, we put the TX antenna at a height of 1.9 m. As the receiver represents a client device such as a notebook or tablet, the receiver is placed at a lower height of 1 m. Both antennas are tilted so that they face each other.

For the PL measurements, we use an omnidirectional TX antenna, and a full angular scan is performed with the directional RX antenna. The TG nodes, used for PL measurements as well as PER and throughput tests, are directed towards each other, i.e., along the direction of the obstructed path. As only reflections that are within an azimuth range of 90° of the obstructed path are captured, we also perform measurements rotating the TX or RX node of the TG sounder. For the throughput measurements, we also measure the effect of human body blockage by obstructing the LOS and NLOS links during the measurement by a male person with a height of 175 cm and a weight of 70 kg.

Figure 3. Living room environment. (**a**) Floor plan; (**b**) Picture of non-Line-of-Sight (NLOS) measurement setup NLOS2 with obstructed path distance 4.7 m.

3. Coverage Prediction Tool

For the coverage prediction, we extend the WHIPP tool presented in [61]. It was first developed for mmWave coverage prediction in the highly metallic environment of a ship

hull where multipath components (MPC) due to reflections are dominant. In residential environments, there is not only reflection on objects, but also diffraction around objects and humans, and transmission through objects. Therefore, we added transmission and diffraction models. As can be seen in Figure 3a, we use a simplified floorplan, where furniture is represented by simple geometric objects, without cm-level accuracy of the environment.

We first present the ray-launching algorithm in Section 3.1. In Section 3.2, the methodology for network performance estimation is presented. The validation of the ray-launching algorithm by comparison to an analytic solver is presented in Section 3.3, Section 3.4 provides the settings for the simulations of the living room.

3.1. Ray-Launching Algorithm

The floor plan is discretized into a finite set of grid points, and at every grid point, we calculate the received power, given a certain access point configuration. For each grid point, we launch rays from the access point in both azimuth (360°) and elevation (180°) planes with a predefined angle increment, and determine the interactions with the environment. An accurate description of the environment and material characteristics is required for the calculation of reflection and transmission losses. An object is characterized by its relative permittivity, and the loss is calculated via Fresnel reflection and transmission coefficients. A lookup table with reflection and transmission losses for a broad set of materials and incidence angles is implemented, for materials for which the permittivity is not defined. The loss values in the lookup table are taken from [62]. The path information of the best paths is stored, including path loss, total distance, and interactions. The ray-launching algorithm is presented in Figure 4.
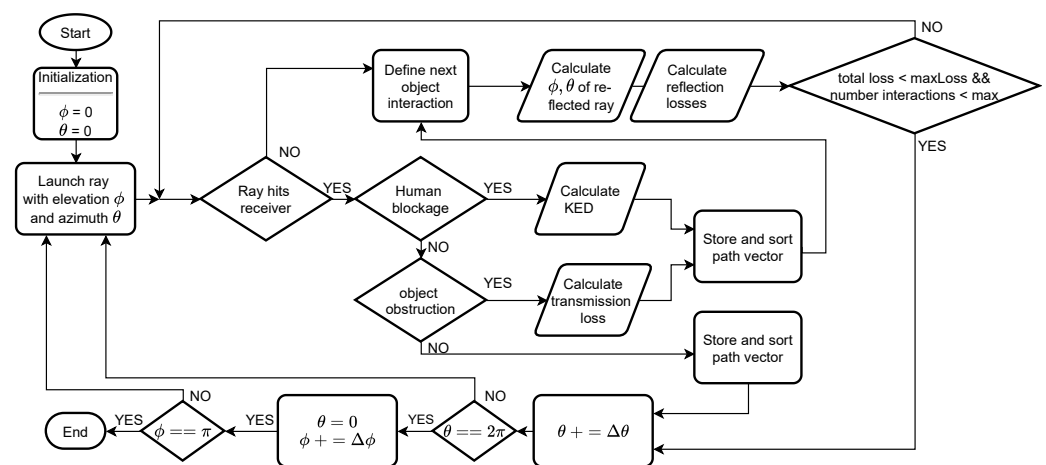
Figure 4. Flowchart presentation of ray-launching algorithm, with elevation angle ϕ, azimuth angle θ, and elevation and azimuth increment $\Delta\phi$, $\Delta\theta$.

For each ray, we first verify whether the ray hits the considered grid point, i.e., whether there is a direct path between the launch point of the ray and the receiver following the considered azimuth and elevation angles. If a direct path exists and is not obstructed, we add it to the path vector. If a direct path exists but is obstructed, we distinguish between an object and human body blockage. Blockage by a human body is modeled via a double knife-edge diffraction (KED) [63]. If an object blocks the direct path, we calculate the transmission loss and add the path information to the path vector. We also consider reflection on the object or body. If no direct ray hits the grid point, we define the next object interaction and calculate the angles of the reflected ray, in both azimuth and elevation fields. Based on the incidence angle, we calculate the reflection losses and add it to the PL of the considered path up to the reflection point. If the total PL does not exceed the maximum PL and the maximum number of interactions are not reached, we perform the same analysis for the departed ray, i.e., verify whether the reflected ray hits the grid point. When the receiver is reached, when the total PL exceeds the maximum PL threshold, or when the number of

interactions reaches its threshold, the next ray is launched from the access point location. We use a receiver margin, i.e., we consider that the receiver is reached when a ray is within a certain distance of the receiver location. The simulation settings are presented in Section 3.4.

The result of the ray-launching algorithm is a path information matrix for every grid point, that contains PL, distance, AoA, AoD, and coordinates for all object interactions of every path between the access point location and grid point. From this matrix, we have the option to investigate omnidirectional PL by summing the received powers from the different MPCs, or to select the path with minimum PL, which makes it more realistic for real network deployments.

We consider an omnidirectional TX antenna, which corresponds to the measurement equipment presented in Section 2.1.1 and is similar to previous work [61]. However, as practical mmWave wireless systems need directional antennas to overcome the high free space PL, we also add antenna directivity to the coverage prediction tool. For this implementation, we need the antenna gain in dBi as a function of azimuth and elevation.

3.2. Throughput Estimation

From the simulated PL, we calculate the received power at every grid point via the inverse of (1), i.e., we subtract PL from the sum of TX power and antenna gains, assuming there are no losses. When a directional antenna is used, the calculated received power for every ray is corrected based on the antenna gain and AoD of the ray. We then select the MCS for which the receiver sensitivity is closest to, but lower than, the calculated received power. Table 1 presents the receiver sensitivities and corresponding data rates for the different MCS indices. These data rates, based on received power, are theoretic values and differ from throughputs based on the MCS selection by an IEEE 802.11ad transceiver.

Table 1. Receiver sensitivity (P_{RS}), modulation, and data rate (DR) used in IEEE 802.11ad for the different modulation and coding schemes (MCS) [1].

MCS	0	1	2	3	4	5	6	7	8	9	10	11	12
P_{RS} [dBm]	−78	−68	−66	−64	−64	−62	−63	−62	−61	−59	−55	−54	−53
Modulation	DBPSK	$\pi/2$-BPSK	$\pi/2$-BPSK	$\pi/2$-BPSK	$\pi/2$-BPSK	$\pi/2$-BPSK	$\pi/2$-QPSK	$\pi/2$-QPSK	$\pi/2$-QPSK	$\pi/2$-QPSK	$\pi/2$-16QAM	$\pi/2$-16QAM	$\pi/2$-16QAM
DR [Mbps]	27.5	385	770	962.5	1155	1251	1540	1925	2310	2502	3080	3850	4620

3.3. Validation

For the validation of the ray-launching algorithm, we compare simulation results for a simple environment to results from FEKO, which is an analytic electromagnetic (EM) wave solver based on the Method of Moments integral formulation of Maxwell's equations. As the room dimension is electrically large considering the high carrier frequency, we use an engine based on the uniform theory of diffraction (UTD), which is a ray-based asymptotic high-frequency numerical method similar to our ray-launching algorithm. We use a room measuring 3 m by 2 m with an L-shaped wall in the middle and define 1 TX location and 4 RX locations, all at the same height. Three RX locations have an NLOS link for which reflected and diffracted paths exist. One RX location has a LOS link. We compare the received power of the EM solver to the ray-launching result. For all RX locations, the estimated power of the ray-launching tool is below the calculated power using the EM solver, with an average offset of 1.4 dB. Not taking into account diffracted paths in the ray-launching algorithm explains the underestimation of the ray-launching tool compared to the EM solver. We also performed simulations with a physical optics (PO) engine, which uses a current-based asymptotic high-frequency numerical method. EM fields are approximated by optical fields using ray optics, and scatterer surfaces are illuminated by an incident current source, which is computed via MoM. To limit the required computational resources, all room dimensions are lowered by a factor of 5, i.e., the outer walls measure 60 cm by 40 cm. The simulations with the PO engine result in lower received powers compared to our ray-launching tool, with an average offset of 6 dB. In [61], we also compare the simulation results using the UTD solver for a larger room, measuring 10 by 6 m, and come to the same conclusions.

3.4. Simulation Settings

Similar to the measurement setup, both antennas are vertically polarized, and the access point is placed at a height of 2 m, whereas the receiver is at a height of 1 m. The parameters used for testing the implementation are summarized in Table 2. To compare the simulation results to the measurements, we perform simulations with the same access point locations as in the experiments. These simulations yield a coverage map with a received power or maximum throughput for every grid point. For the grid points corresponding to the RX antenna locations of the measurements, we store all propagation paths. The maximum PL threshold is set to 140 dB. The maximum number of reflections is set to 5, but it should be noted that the number of paths consisting of 5 reflections and still having a PL less than 140 dB is limited.

Table 2. Simulation parameters coverage prediction tool.

Parameter	Value
Grid size	20 cm
Receiver margin	10 cm
Angular resolution	$\pi/48$
Maximum PL	140 dB
Maximum # reflections	5
Transmit power	15 dBm

4. Results and Discussion

Table 3 summarizes the overall measurement and simulation results for the three scenarios, i.e., one LOS scenario and two NLOS scenarios. $PL_{min,meas}$ is the minimum measured PL at 60 GHz over all AoAs, measured with the spectrum analyzer-based sounder. $PL_{omni,meas}$ is the omnidirectional PL, by interpolating and summing the received powers over all AoAs. Based on the angular PL measurements, the angular spread (AS) is obtained. $PL_{min,TG}$ is the minimum measured PL using the TG platform, i.e., the PL of the TX-RX beam configuration for which the PL is minimal. $PL_{min,sim}$ is the total PL of the best path from the ray-launching simulations.

In the next sections, we discuss the measurement and simulation results in detail, starting with the angular PL measurements, continuing with PER measurements and throughput estimation, and concluding with the simulation results from the coverage prediction tool.

Table 3. Summary of measurement and simulation results for the different scenarios, with $PL_{min,meas}$ the minimum measured PL, $PL_{omni,meas}$ the omnidirectional measured PL, AS the measured angular spread, $PL_{min,TG}$ the minimum measured PL using the TG platform, and $PL_{min,sim}$ the minimum simulated PL.

| Scenario	$PL_{min,meas}$	$PL_{omni,meas}$	AS	$PL_{min,TG}$	$PL_{min,sim}$
LOS	83.1 dB	81.8 dB	30.5°	82.9 dB	83.0 dB
NLOS 1	88.7 dB	87.0 dB	52.8°	87.5 dB	97.5 dB
NLOS 2	95.6 dB	92.1 dB	65.0°	106.1 dB	92.4 dB

4.1. Angular Path Loss

Figure 5 shows the angular PL measurement results at 60 GHz for the three scenarios, using the spectrum analyzer-based channel sounder. For the LOS scenario, the minimum PL is 83.1 dB and corresponds to FSPL for a distance of 4.7 m. The minimum PL corresponds to the direct path with AoA 0°, but first-order wall reflections are visible in the angular profile. Measured PL is 98.7 dB at AoA 84° and 99.7 dB at AoA 132°. There is also a reflection at AoA −96° on wooden furniture, with a corresponding PL of 109.2 dB. The mean AoA is 6.9° and the RMS angular spread is 30.5°. Omnidirectional PL for the LOS

scenario is 81.8 dB. For scenario NLOS1, with an obstructed LOS path with a distance of 4.7 m, the minimum PL is only slightly higher than the FSPL, i.e., 88.7 dB for AoA 96°, which corresponds to a first-order wall reflection. A path around the corner, with AoA 12°, has a PL of 92.6 dB. Omnidirectional PL is slightly lower, i.e., 87.0 dB. The diffracted path is the path with minimum PL for scenario NLOS2, with a PL of 95.6 dB for AoA −60°. A first-order wall reflection occurs at AoA −144°, with PL 101.7 dB. The minimum PL of 95.6 dB is found for AoA −50°, and omnidirectional PL is 92.1 dB, The mean AoA values for the two NLOS scenarios are 71.4° and −47.0°, respectively, the RMS angular spread values of 52.8° and 65.0°, respectively, are higher than for the LOS scenario. These RMS angular spread values are larger than the azimuth angular spread values of 15.6° for a small office room reported in [15] and 14.5° for a corridor environment in [18]. On the other hand, the LOS RMS angular spread is smaller than the measured LOS angular spread of 39.1° at 28 GHz in a larger office environment [31].
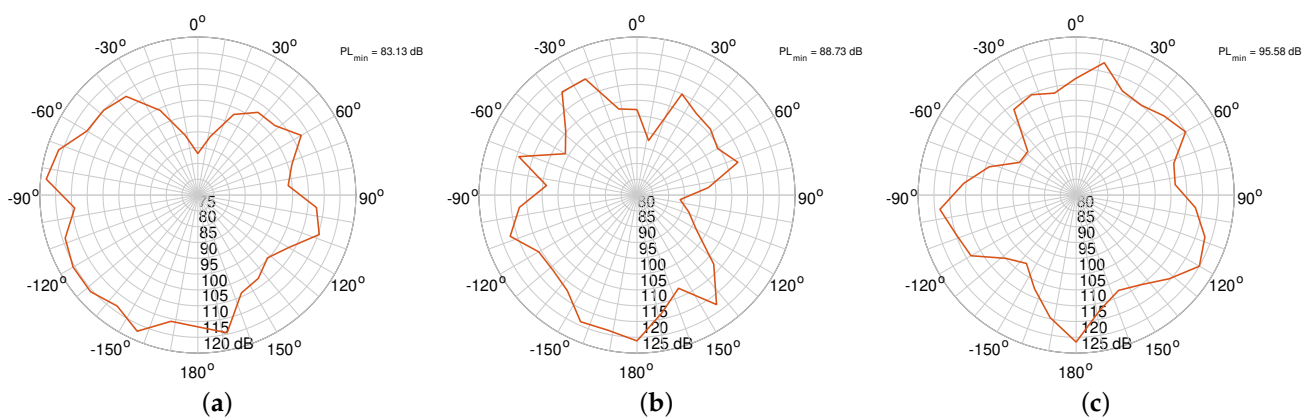
Figure 5. Angular path loss profiles at 60 GHz for Line-of-Sight (LOS) and non-Line-of-Sight (NLOS) scenarios. (**a**) LOS, distance 4.7 m; (**b**) NLOS, distance 4.7 m; (**c**) NLOS, distance 3.4 m.

Figure 6 presents the PL as a function of frequency for the 3 scenarios. For each scenario, we show PL for the best path, i.e., for the AoA for which the PL is minimal. As expected, PL increases with frequency, and the measured PL for the LOS link corresponds to the FSPL, considering the gain variations of the measurement antennas. Surprisingly, PL for the shorter link NLOS2 is higher than for the longer link NLOS1. The frequency variations are larger than the gain variation of 2 dB, which shows the frequency selectivity of the channel.
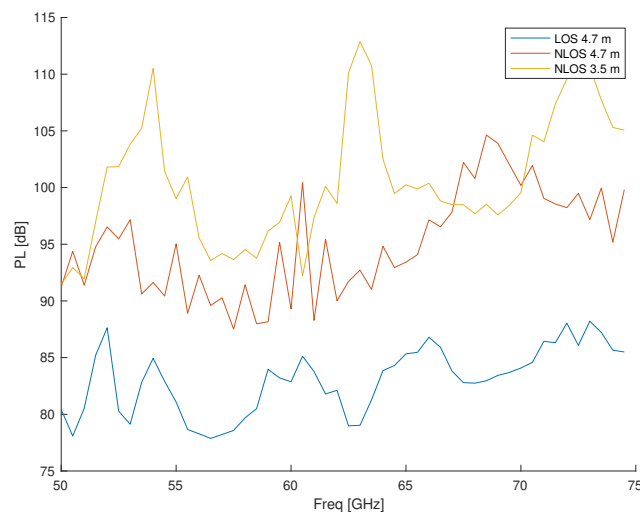
Figure 6. Measured path loss as a function of frequency for angle of arrival (AoA) with minimum PL at 60 GHz.

The indoor 3GPP LOS PL model estimates a PL value of 79.6 dB which is a slight underestimation of the measured omnidirectional PL of 81.8 dB, whereas the ITU-R P.1238 PL model for an office environment slightly overestimates PL, with a PL of 82.3 dB for distance 4.7 m. FSPL is a better fit based on the measurement result. The PL estimation of scenario NLOS2 using the indoor 3GPP NLOS PL model yields 87.3 dB which corresponds to the measured PL.

4.2. Path Loss, Packet Error Rate, and Throughput Estimation Measurements Using TG Platform

We use the TG platform for directional PL measurements, as well as PER measurements and a maximum throughput estimation based on the transceiver's adaptive rate implementation, i.e., MCS selection. An angular scan is performed over an azimuthal range of 90° at the TX and RX nodes. From the angular scan, we select the TX-RX beam combination with minimum PL. For the LOS link, this is the beam with AoD and AoA 0°, with PL 82.9 dB. The SNR of the frames is 20 dB, which results in an estimated throughput of 4.62 Gbps. One reflected path is measured with the TG platform, with a PL of 100 dB, and an AoD and AoA of 40°. The SNR for this reflected component is 12 dB.

For link NLOS1, with both nodes positioned in the direction of the obstructed LOS path, the minimum PL of 105.2 dB is found for a beam combination TX −25.3° and RX −32.3°. If we rotate the nodes, both facing in the direction of window 3, the minimum PL decreases to 87.5 dB, as can be seen in Figure 7. This path corresponds to a first-order reflection on the window and the corresponding SNR of 15 dB allows a maximum PHY data rate of 3.85 Gbps. Reflections on the wall are also visible in the angular PL profile, e.g., with PL 98 dB for TX 35.2° and RX 22.5°. For link NLOS2, the minimum PL of 106 dB is found for AoD 47.8° and AoA 53.4°, i.e., via a first-order wall reflection. The SNR of 10 dB also results in a throughput of 3.85 Gbps. The minimum PL for the NLOS scenarios, measured with the TG platform, is higher than the minimum PL measured with the channel sounder. By using an omnidirectional transmit antenna with the channel sounder, more reflected power is received, whereas with the double-directional TG platform (and sequential beamsteering), less transmitted power is received.
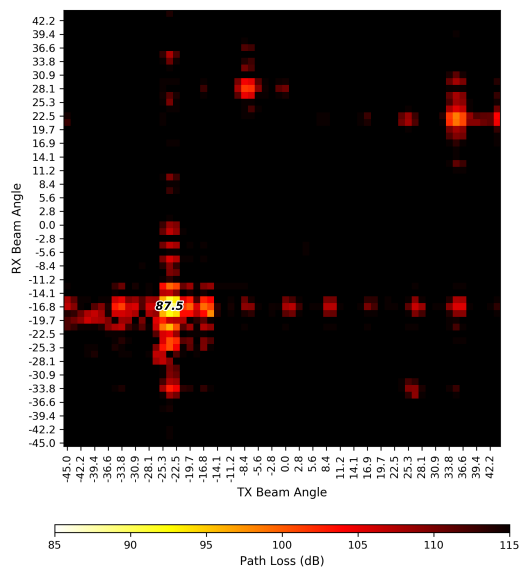

Figure 7. Angular path loss profile measured with Terragraph platform for link NLOS1 with distance 4.7 m.

As no adaptive beamforming is used, the estimated throughput drops when a person obstructs the communication link. For the LOS link, the PL increases from 83 dB to 120 dB, which is in line with the human blockage model from [35], and the SNR decreases from 20 dB to 3 dB. The decreased SNR results in a throughput estimate decrease from 4.62 Gbps to 962 Mbps. It only decreases to 3.85 Gbps if the reflected path is used, with AoD and

AoA 40°. When a person obstructs the reflected path for the NLOS scenarios, the SNR also decreases to 3 dB. The throughput decreases to 962 Mbps.

Figure 8 shows the measured PER as a function of the MCS index. For the LOS link, the packet error rate is below 4% for all MCS indices. For the NLOS scenarios, the PER starts increasing from MCS index 4. E.g., for link NLOS2, there is 50% packet loss for MCS index 6. Starting from MCS index 7, all packets are lost. The PER measurements indicate that the throughput estimation of the TG sounder, which is based on the measured SNR, is optimistic, but even for NLOS scenarios, a throughput exceeding 1.25 Gbps is expected, i.e., a data rate corresponding to MCS index 5.
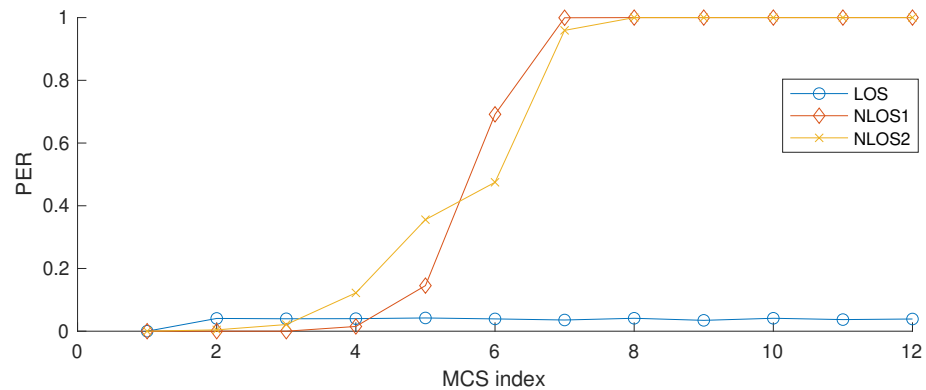
Figure 8. Measured packet error rate as a function of modulation and coding scheme index for the different measurement scenarios.

4.3. Coverage Prediction via Ray-Tracing

We performed simulations using the ray-launching algorithm presented in Section 3 for access point locations corresponding to the TX antenna locations used in the measurements, and we analyzed the multipath components for a grid point corresponding to the RX locations used in the measurements. The simulation time using the settings from Table 2 is 67 min on a notebook computer with a 2.3 GHz Intel Core i5 processor.

4.3.1. Line-of-Sight

For a simulation with the same TX and RX location as in the LOS measurement, the minimum PL of 82 dB corresponds to the direct LOS path and is equal to the measured PL. Two paths exist with a total PL of 97 dB, i.e., the path via a first-order ceiling reflection, as well as the path with reflections on windows 3 and 4. This last path corresponds to the measured PL of 99 dB using the channel sounder, with AoA 132°. With the TG platform, we have not measured this path, as it is outside the 90° azimuth scanning range. Ceiling reflections were not measured with the channel sounder or TG platform, due to the limited HPBW in the elevation plane. A path with reflection on furniture, followed by a reflection on window 2 and a ground reflection, has a PL of 99 dB. Two paths have a PL of 111 dB. We conclude that simulated PL corresponds well to measured PL, even though we do not have a detailed representation of the environment. The throughput estimation of 4.62 Gbps, when using a TX power of 13 dBm and antenna gain of 20 dBi, corresponds to the throughput estimation using the TG platform, and is in line with the PER measurement results.

4.3.2. Non-Line-of-Sight Link NLOS1

Figure 9 shows the coverage map with the received power at every grid point for the access point located at the same location as the TX antenna of scenario NLOS1. In Figure 9a, an omnidirectional TX antenna with a gain of 3 dBi is considered, which is equivalent to the PL measurement setup, whereas in Figure 9b a directional TX antenna with a gain of 23 dBi and an HPBW of 18° is considered, which is similar to the horn antenna used as RX antenna in the PL measurement setup. Figure 9a also visualizes the best reflected

paths. The simulated minimum PL at the grid point corresponding to the RX antenna of scenario NLOS1 is the same for the omnidirectional and directional antennas, but the throughput estimation takes into account the antenna gain, which is higher for a directional antenna, and therefore the directional antenna has an advantage. Two paths exist with a minimum PL of 98 dB. The first path consists of a ceiling reflection, the second path reflects on the wall of the upper-right corner, i.e., from where the photograph in Figure 3b is taken. This second path is also captured with the TG platform, i.e., TX beam 35.2°, RX beam 22.5° with PL 98.4 dB, as can be seen in Figure 7. Two paths have a total PL of 111 dB. The first path undergoes three reflections with a small incident angle (two wall reflections and one window reflection) before reaching the receiver. The second path undergoes five reflections, including one ceiling reflection. Two more paths, with PL values of 117 dB and 120 dB, undergo five reflections. For this scenario, the ray-launching algorithm misses the reflected path with AoA 95° and PL 87 dB, as well as the diffracted path with AoA 11°. The throughput estimation for the grid point corresponding to the RX location of NLOS1, is 2.5 Gbps, which is lower than the throughput based on SNR (3.85 Gbps) but larger than the estimation based on PER (1.25 Gbps).
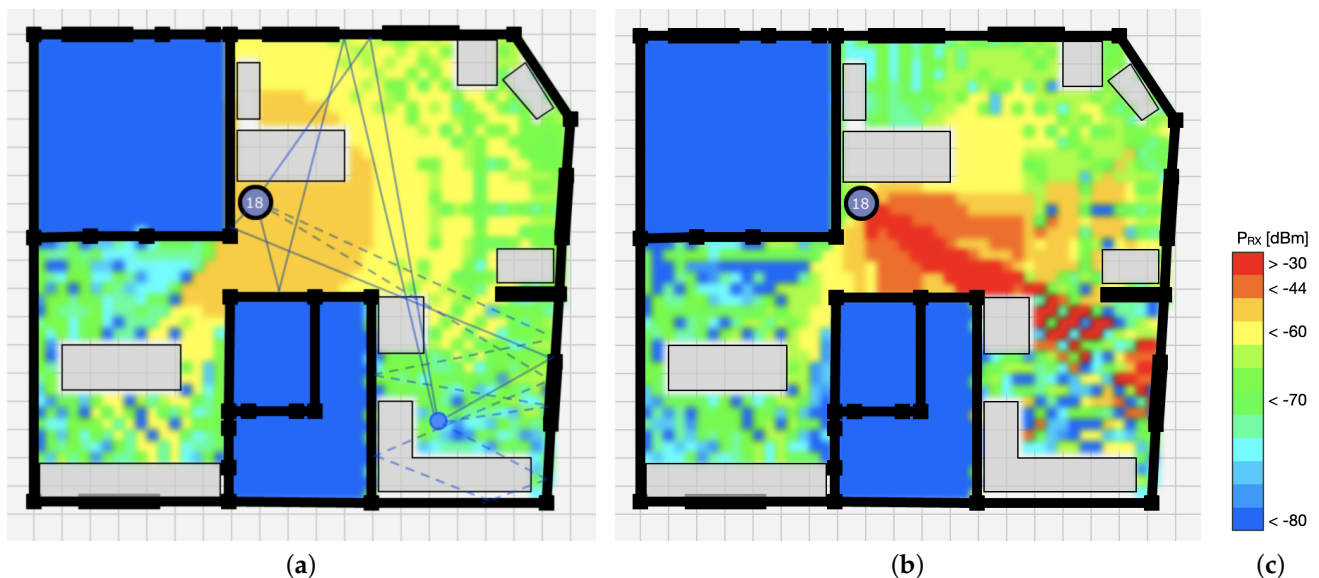
Figure 9. Received power prediction using ray-launching algorithm, for an access point location identical to the TX antenna location used in the NLOS1 path loss measurements. (**a**) Omnidirectional antenna with 3 dBi gain. Full lines represent the best reflected paths, and dashed lines represent paths with ceiling reflections. (**b**) Directional antenna with 23 dBi gain. (**c**) Legend.

4.3.3. Non-Line-of-Sight Link Nlos2

For link NLOS2, the PL of the first-order wall reflection is 92.4 dB, with a path length of 6.4 m. This corresponds well to the angular PL measurement. The reflected path via a ceiling and wall reflection has a PL of 98 dB, and the path via a reflection on window 4, followed by a wall reflection and another window reflection (on window 5), has a PL of 104 dB. Three more paths involve a ceiling reflection and multiple wall reflections, with PL values ranging from 107 dB to 125 dB.

The throughput estimation for the grid point corresponding to the RX location of NLOS2, is 2.5 Gbps, which is lower than the estimation based on SNR (3.85 Gbps), but higher than the throughput based on PER (1.15 Gbps).

4.3.4. Human Body Shadowing

A human body obstructing the LOS path causes significant attenuation, with additional losses up to 20 dB. The simulated PL decreases by 10 dB at the shadow border when

taking into account diffraction loss using a double KED model, which corresponds to the measurements using the TG platform. However, if we take into account reflection in the PL simulations, the path with minimum PL is mostly a reflected path. We conclude that the simulation time decreases with a limited impact on simulation accuracy by not taking diffraction into account. For simulation of a fixed link, i.e., when estimating the performance of a system without adaptive beamsteering, the diffraction model is needed.

5. Conclusions

In this paper, we have presented V-band measurements in an indoor residential environment. Angular PL measurements are performed for both LOS and NLOS scenarios, as well as PER and throughput estimation measurements at 60 GHz using IEEE 802.11ad nodes. The channel model is implemented in a ray-launching algorithm used for simulating network performance, including coverage and throughput, based on a pre-defined access point location.

The angular PL measurements using a spectrum analyzer-based channel sounder with an omnidirectional TX antenna show that multiple reflections are received, via wall and window reflections. Double-directional angular PL, measured via the TG platform, differs from the angular PL measurements, as the TG platform only scans the azimuth plane over a sector of 90°. In the network performance simulation tool, rays are launched in both azimuth and elevation planes, and multipath components are present that were not captured via the channel sounder or TG platform, e.g., the floor and ceiling reflections, due to the antenna radiation patterns and polarizations. When taking the transmitter's antenna radiation pattern into account, simulation results correspond to the measurement results using the TG platform, whereas a generic indoor model underestimates PL. Simulated throughput corresponds well to the throughput obtained via the TG platform for LOS scenarios, whereas for NLOS scenarios, the simulated throughput is lower. Furthermore, PER measurements show that the maximum simulated throughput cannot be obtained.

Future work includes further optimization of the ray-launching algorithm by taking into account spatial correlation of multipath components so that it is not necessary to not perform the full algorithm for every single grid point. When the simulation time is lowered, a heuristic will be deployed to perform network planning, i.e., define the optimal location of the access point. Furthermore, the current implementation is only applicable for vertically or horizontally polarized antennas and does not consider de-polarization effects of reflection and transmission. This could be extended to allow generic polarizations, i.e., allow the antennas to be rotated in the three-dimensional space.

Author Contributions: Conceptualization, B.D.B. and A.A.; methodology, B.D.B. and D.P.; software, B.D.B., A.A. and D.P.; validation, B.D.B. and A.A.; formal analysis, B.D.B.; investigation, B.D.B.; resources, W.J.; data curation, B.D.B.; writing—original draft preparation, B.D.B.; writing—review and editing, D.P. and W.J.; visualization, B.D.B.; supervision, D.P.; project administration, W.J.; funding acquisition, W.J. All authors have read and agreed to the published version of the manuscript.

Institutional Review Board Statement: Not applicable.

Informed Consent Statement: Not applicable.

Data Availability Statement: The data presented in this study, as well as the processing scripts, are made available in the NIST NextG Channel Model Alliance Database.

Conflicts of Interest: The authors declare no conflict of interest.

Abbreviations

The following abbreviations are used in this manuscript:

3GPP	Third Generation Partnership Project
5G	Fifth generation
AoA	Angle of arrival
AoD	Angle of departure
DANL	Displayed average noise level
EIRP	Effective isotropically radiated power
EM	Electromagnetic
FSPL	Free space path loss
HPBW	Half power beam width
IEEE	Institute of Electrical and Electronics Engineers
IF	Intermediate frequency
ISM	Industrial, scientific, and medical
ITU	International Telecommunication Union
KED	Knife-edge diffraction
LOS	Line-of-sight
MAC	Medium Access Control
MCS	Modulation and coding scheme
MDPI	Multidisciplinary Digital Publishing Institute
MIMO	Multiple-Input Multiple-Output
MoM	Method of moments
MPC	Multipath components
NLOS	Non-line-of-sight
PER	Packet error rate
PHY	physical layer
PL	Path loss
PO	Physical optics
RF	Radio frequency
RSSI	Received signal strength information
RX	Receiving
RMS	Root mean squared
SNR	Signal to noise ratio
TCP	Transmission Control Protocol
TG	Terragraph
TX	Transmitting
UTD	Uniform theory of diffraction

References

1. *IEEE 802.11ad-2012;* IEEE Standard for Information Technology—Telecommunications and Information Exchange between Systems—Local and Metropolitan Area Networks—Specific Requirements-Part 11: Wireless LAN Medium Access Control (MAC) and Physical Layer (PHY) Specifications Amendment 3: Enhancements for Very High Throughput in the 60 GHz Band. IEEE Computer Society: Washington, DC, USA, 2012.
2. *IEEE 802.11ay-2021;* IEEE Standard for Information Technology—Telecommunications and Information Exchange between Systems Local and Metropolitan Area Networks—Specific Requirements Part 11: Wireless LAN Medium Access Control (MAC) and Physical Layer (PHY) Specifications Amendment 2: Enhanced Throughput for Operation in License-exempt Bands above 45 GHz. IEEE Computer Society: Washington, DC, USA, 2021.
3. Maltsev, A.; Pudeyev, A.; Lomayev, A.; Bolotin, I. Channel modeling in the next generation mmWave Wi-Fi: IEEE 802.11ay standard. In Proceedings of the European Wireless 2016 22th European Wireless Conference, Oulu, Finland, 18–20 May 2016; pp. 1–8.
4. ITU-R. *Multiple Gigabit Wireless Systems in Frequencies around 60 GHz*; Technical Report, ITU-R M.2003-2; ITU-R: Geneva, Switzerland, 2018.
5. Aslam, M.Z.; Corre, Y.; Belschner, J.; Arockiaraj, G.S.; Jäger, M. Analysis of 60-GHz In-street Backhaul Channel Measurements and LiDAR Ray-based Simulations. In Proceedings of the 2020 14th European Conference on Antennas and Propagation (EuCAP), Copenhagen, Denmark, 15–20 March 2020; pp. 1–5. [CrossRef]
6. Du, J.; Chizhik, D.; Feick, R.; Castro, G.; Rodríguez, M.; Valenzuela, R.A. Suburban Residential Building Penetration Loss at 28 GHz for Fixed Wireless Access. *IEEE Wirel. Commun. Lett.* **2018**, *7*, 890–893. [CrossRef]

7. Zhao, X.; Li, S.; Wang, Q.; Wang, M.; Sun, S.; Hong, W. Channel Measurements, Modeling, Simulation and Validation at 32 GHz in Outdoor Microcells for 5G Radio Systems. *IEEE Access* **2017**, *5*, 1062–1072. [CrossRef]

8. 3GPP. *Study on Channel Model for Frequencies from 0.5 to 100 GHz.* 2019. Available online: https://portal.3gpp.org/desktopmodules/Specifications/SpecificationDetails.aspx?specificationId=3173 (accessed on 30 December 2021).

9. Salhi, M.A.; Kleine-Ostmann, T.; Schrader, T. Propagation Channel Measurements in the mm- and Sub-mm Wave Range for Different Indoor Communication Scenarios. *J. Infrared Millim. Terahertz Waves* **2021**, *42*, 357–370. [CrossRef]

10. Kibilda, J.; MacKenzie, A.B.; Abdel-Rahman, M.J.; Yoo, S.K.; Giordano, L.G.; Cotton, S.L.; Marchetti, N.; Saad, W.; Scanlon, W.G.; Garcia-Rodriguez, A.; et al. Indoor Millimeter-Wave Systems: Design and Performance Evaluation. *Proc. IEEE* **2020**, *108*, 923–944. [CrossRef]

11. Raghavan, V.; Partyka, A.; Akhoondzadeh-Asl, L.; Tassoudji, M.A.; Koymen, O.H.; Sanelli, J. Millimeter Wave Channel Measurements and Implications for PHY Layer Design. *IEEE Trans. Antennas Propag.* **2017**, *65*, 6521–6533. [CrossRef]

12. De Beelde, B.; Tanghe, E.; Yusuf, M.; Plets, D.; Joseph, W. Radio Channel Modelling in a Ship Hull: Path Loss at 868 MHz, 2.4 GHz, 5.25 GHz and 60 GHz. *IEEE Antennas Wirel. Propag. Lett.* **2021**, *20*, 597–601 [CrossRef]

13. Kyro, M.; Haneda, K.; Simola, J.; Nakai, K.; Takizawa, K.i.; Hagiwara, H.; Vainikainen, P. Measurement Based Path Loss and Delay Spread Modeling in Hospital Environments at 60 GHz. *IEEE Trans. Wirel. Commun.* **2011**, *10*, 2423–2427. [CrossRef]

14. Davies, R.; Bensebti, M.; Beach, M.; McGeehan, J. Wireless propagation measurements in indoor multipath environments at 1.7 GHz and 60 GHz for small cell systems. In Proceedings of the 41st IEEE Vehicular Technology Conference, St. Louis, MO, USA, 19–22 May 1991; pp. 589–593. [CrossRef]

15. Dupleich, D.; Fuschini, F.; Mueller, R.; Vitucci, E.; Schneider, C.; Degli Esposti, V.; Thomä, R. Directional characterization of the 60 GHz indoor-office channel. In Proceedings of the 2014 XXXIth URSI General Assembly and Scientific Symposium (URSI GASS), Beijing, China, 16–23 August 2014; pp. 1–4. [CrossRef]

16. Maltsev, A.; Maslennikov, R.; Sevastyanov, A.; Khoryaev, A.; Lomayev, A. Experimental investigations of 60 GHz WLAN systems in office environment. *IEEE J. Sel. Areas Commun.* **2009**, *27*, 1488–1499. [CrossRef]

17. Maltsev, A.; Maslennikov, R.; Sevastyanov, A.; Lomayev, A.; Khoryaev, A. Statistical channel model for 60 GHz WLAN systems in conference room environment. In Proceedings of the Fourth European Conference on Antennas and Propagation, Barcelona, Spain, 12–16 April 2010; pp. 1–5.

18. Choi, M.S.; Grosskopf; Rohde. Statistical Characteristics of 60 GHz Wideband Indoor Propagation Channel. In Proceedings of the 2005 IEEE 16th International Symposium on Personal, Indoor and Mobile Radio Communications, Berlin, Germany, 11–14 September 2005; Volume 1, pp. 599–603. [CrossRef]

19. Hao, X.; Kukshya, V.; Rappaport, T.S. Spatial and temporal characteristics of 60-GHz indoor channels. *IEEE J. Sel. Areas Commun.* **2002**, *20*, 620–630. [CrossRef]

20. Maccartney, G.R.; Rappaport, T.S.; Sun, S.; Deng, S. Indoor Office Wideband Millimeter-Wave Propagation Measurements and Channel Models at 28 and 73 GHz for Ultra-Dense 5G Wireless Networks. *IEEE Access* **2015**, *3*, 2388–2424. [CrossRef]

21. Al-Saman, A.; Cheffena, M.; Elijah, O.; Al-Gumaei, Y.A.; Abdul Rahim, S.K.; Al-Hadhrami, T. Survey of Millimeter-Wave Propagation Measurements and Models in Indoor Environments. *Electronics* **2021**, *10*, 1653. [CrossRef]

22. Yang, H.; Smulders; Herben. Indoor Channel Measurements and Analysis in the Frequency Bands 2 GHz and 60 GHz. In Proceedings of the 2005 IEEE 16th International Symposium on Personal, Indoor and Mobile Radio Communications, Berlin, Germany, 11–14 September 2005; Volume 1, pp. 579–583. [CrossRef]

23. Yang, H.; Herben, M.; Smulders, P. Impact of antenna pattern and reflective environment on 60 GHz indoor radio channel characteristics. *IEEE Antennas Wirel. Propag. Lett.* **2005**, *4*, 300–303. [CrossRef]

24. Wu, X.; Wang, C.; Sun, J.; Huang, J.; Feng, R.; Yang, Y.; Ge, X. 60-GHz Millimeter-Wave Channel Measurements and Modeling for Indoor Office Environments. *IEEE Trans. Antennas Propag.* **2017**, *65*, 1912–1924. [CrossRef]

25. Khawaja, W.; Ozdemir, O.; Yapici, Y.; Erden, F.; Guvenc, I. Coverage Enhancement for NLOS mmWave Links Using Passive Reflectors. *IEEE Open J. Commun. Soc.* **2020**, *1*, 263–281. [CrossRef]

26. Kim, B.; Kim, H.; Choi, D.; Lee, Y.; Hong, W.; Park, J. 28 GHz propagation analysis for passive repeaters in NLOS channel environment. In Proceedings of the 2015 9th European Conference on Antennas and Propagation (EuCAP), Lisbon, Portugal, 13–17 April 2015; pp. 1–4.

27. Anjinappa, C.K.; Erden, F.; Güvenç, I. Base Station and Passive Reflectors Placement for Urban mmWave Networks. *IEEE Trans. Veh. Technol.* **2021**, *70*, 3525–3539. [CrossRef]

28. Haneda, K.; Järveläinen, J.; Karttunen, A.; Kyrö, M.; Putkonen, J. A Statistical Spatio-Temporal Radio Channel Model for Large Indoor Environments at 60 and 70 GHz. *IEEE Trans. Antennas Propag.* **2015**, *63*, 2694–2704. [CrossRef]

29. Kelner, J.M.; Ziółkowski, C.; Uljasz, B. Comparison of angular spread for 6 and 60 GHz based on 3GPP standard. In Proceedings of the 2018 22nd International Microwave and Radar Conference (MIKON), Poznan, Poland, 14–17 May 2018; pp. 286–290. [CrossRef]

30. Pometcu, L.; D'Errico, R. Characterization of sub-THz and mmwave propagation channel for indoor scenarios. In Proceedings of the 12th European Conference on Antennas and Propagation (EuCAP 2018), London, UK, 9–13 April 2018; pp. 1–4. [CrossRef]

31. Ju, S.; Xing, Y.; Kanhere, O.; Rappaport, T.S. Millimeter Wave and Sub-Terahertz Spatial Statistical Channel Model for an Indoor Office Building. *IEEE J. Sel. Areas Commun.* **2021**, *39*, 1561–1575. [CrossRef]

32. De Beelde, B.; Tanghe, E.; Desset, C.; Bourdoux, A.; Plets, D.; Joseph, W. Office Room Channel Modeling and Object Attenuation at Sub-THz Frequencies. *Electronics* **2021**, *10*, 1725. [CrossRef]

33. Collonge, S.; Zaharia, G.; El Zein, G. Influence of the human activity on the propagation characteristics of 60 GHz indoor channels. In Proceedings of the 7th IEEE Semiannual Vehicular Technology Conference, 2003. VTC 2003-Spring, Jeju, Korea, 22–25 April 2003; Volume 1, pp. 251–255. [CrossRef]

34. Collonge, S.; Zaharia, G.; Zein, G. Influence of the human activity on wide-band characteristics of the 60 GHz indoor radio channel. *IEEE Trans. Wirel. Commun.* **2004**, *3*, 2396–2406. [CrossRef]

35. Jacob, M.; Priebe, S.; Kürner, T.; Peter, M.; Wisotzki, M.; Felbecker, R.; Keusgen, W. Extension and validation of the IEEE 802.11ad 60 GHz human blockage model. In Proceedings of the 2013 7th European Conference on Antennas and Propagation (EuCAP), 2013, Gothenburg, Sweden, 8–12 April 2013; pp. 2806–2810.

36. Hicheri, R.; Pätzold, M.; Youssef, N. Estimation of the Velocity of a Walking Person in Indoor Environments from mmWave Signals. In Proceedings of the 2018 IEEE Globecom Workshops (GC Wkshps), Abu Dhabi, United Arab Emirates, 9–13 December 2018; pp. 1–7. [CrossRef]

37. Collonge, S.; Zaharia, G.; El Zein, G. Influence of the furniture on 60 GHz radio propagation in a residential environment. In Proceedings of the Signals, Circuits and Systems, Iasi, Romania, 10–11 July 2003; Volume 2, pp. 413–416. [CrossRef]

38. Mudonhi, A.; D'Errico, R.; Oestges, C. Indoor mmWave Channel Characterization with Large Virtual Antenna Arrays. In Proceedings of the 2020 14th European Conference on Antennas and Propagation (EuCAP), Copenhagen, Denmark, 15–20 March 2020; pp. 1–5. [CrossRef]

39. Karstensen, A.; Wei, F.; Carton, I.; Pedersen, G.F. Comparison of ray tracing simulations and channel measurements at mmWave bands for indoor scenarios. In Proceedings of the 2016 10th European Conference on Antennas and Propagation (EuCAP), Davos, Switzerland, 10–15 April 2016; pp. 1–5. [CrossRef]

40. Shen, Y.; Shao, Y.; Xi, L.; Zhang, H.; Zhang, J. Millimeter-Wave Propagation Measurement and Modeling in Indoor Corridor and Stairwell at 26 and 38 GHz. *IEEE Access* **2021**, *9*, 87792–87805. [CrossRef]

41. Schmieder, M.; Eichler, T.; Wittig, S.; Peter, M.; Keusgen, W. Measurement and Characterization of an Indoor Industrial Environment at 3.7 and 28 GHz. In Proceedings of the 2020 14th European Conference on Antennas and Propagation (EuCAP), Copenhagen, Denmark, 15–20 March 2020; pp. 1–5. [CrossRef]

42. Sheeba Kumari, M.; Rao, S.A.; Kumar, N. Modeling and Link Budget Estimation of Directional mmWave Outdoor Environment for 5G. In Proceedings of the 2019 European Conference on Networks and Communications (EuCNC), Valencia, Spain, 18–21 June 2019; pp. 106–111. [CrossRef]

43. Naqvi, S.H.R.; Ho, P.H. Achieving 5G NR mmWave Indoor Coverage Under Integrated Access Backhaul. *IEEE Syst. J.* **2021**, *15*, 1–11. [CrossRef]

44. Naqvi, S.H.R.; Ho, P.H.; Peng, L. 5G NR mmWave indoor coverage with massive antenna system. *J. Commun. Netw.* **2021**, *23*, 1–11. [CrossRef]

45. Legg, P.; McConnell, R. Meshed Backhauling of Small Cells Using IEEE802.11ad at 60 GHz. In Proceedings of the 2018 European Conference on Networks and Communications (EuCNC), Ljubljana, Slovenia, 18–21 June 2018; pp. 393–397. [CrossRef]

46. El-Yamany, A.; Petri, M. An Adaptive IEEE 802.11ad Indoor mmWave Inner-Receiver Architecture. In Proceedings of the 2018 2nd URSI Atlantic Radio Science Meeting (AT-RASC), Gran Canaria, Spain, 28 May–1 June 2018; pp. 1–4. [CrossRef]

47. Gebreyohannes, F.T.; Frappé, A.; Kaiser, A. A Configurable Transmitter Architecture for IEEE 802.11ac and 802.11ad Standards. *IEEE Trans. Circuits Syst. II Express Briefs* **2016**, *63*, 9–13. [CrossRef]

48. Saito, N.; Tsukizawa, T.; Shirakata, N.; Morita, T.; Tanaka, K.; Sato, J.; Morishita, Y.; Kanemaru, M.; Kitamura, R.; Shima, T.; et al. A Fully Integrated 60-GHz CMOS Transceiver Chipset Based on WiGig/IEEE 802.11ad With Built-In Self Calibration for Mobile Usage. *IEEE J. Solid State Circuits* **2013**, *48*, 3146–3159. [CrossRef]

49. Zaaimia, M.; Touhami, R.; Hamza, A.; Yagoub, M.C.E. Design and performance evaluation of 802.11ad phys in 60 GHz multipath fading channel. In Proceedings of the 2013 8th International Workshop on Systems, Signal Processing and their Applications (WoSSPA), Algiers, Algeria, 12–15 May 2013; pp. 521–525. [CrossRef]

50. Chandra, K.; Prasad, R.V.; Niemegeers, I. Performance Analysis of IEEE 802.11ad MAC Protocol. *IEEE Commun. Lett.* **2017**, *21*, 1513–1516. [CrossRef]

51. Nino, R.; Nishio, T.; Murase, T. Throughput Measurement for IEEE 802.11ad with Various Obstacles and Reflectors by Real Machines. In Proceedings of the 2021 IEEE 3rd Global Conference on Life Sciences and Technologies (LifeTech), Nara, Japan, 9–11 March 2021; pp. 401–402. [CrossRef]

52. Hirata, T.; Murase, T. Throughput Measurement of IEEE 802.11ad with Various Interferences on Vehicles. In Proceedings of the 2020 IEEE International Conference on Consumer Electronics-Taiwan (ICCE-Taiwan), Taoyuan, Taiwan, 28–30 September 2020; pp. 1–2. [CrossRef]

53. Saha, S.K.; Garg, A.; Koutsonikolas, D. A first look at TCP performance in indoor IEEE 802.11ad WLANs. In Proceedings of the 2015 IEEE Conference on Computer Communications Workshops (INFOCOM WKSHPS), Hong Kong, China, 26 April–1 May 2015; pp. 63–64. [CrossRef]

54. Shkel, A.; Mehrabani, A.; Kusuma, J. A Configurable 60 GHz Phased Array Platform for Multi-Link mmWave Channel Characterization. In Proceedings of the 2021 IEEE International Conference on Communications Workshops (ICC Workshops), Montreal, QC, Canada, 14–23 June 2021; pp. 1–6. [CrossRef]

55. Garcia Sanchez, S.; Mohanti, S.; Jaisinghani, D.; Chowdhury, K.R. Millimeter-wave Base Stations in the Sky: An Experimental Study of UAV-to-Ground Communications. *IEEE Trans. Mob. Comput.* **2020**, *21*, 1. [CrossRef]

56. Sanchez, S.G.; Chowdhury, K.R. Robust 60 GHz Beamforming for UAVs: Experimental Analysis of Hovering, Blockage and Beam Selection. *IEEE Internet Things J.* **2020**, *8*, 9838–9854. [CrossRef]

57. Tariq, M.H.; Chondroulis, I.; Skartsilas, P.; Babu, N.; Papadias, C.B. mmWave Massive MIMO Channel Measurements for Fixed Wireless and Smart City Applications. In Proceedings of the 2020 IEEE 31st Annual International Symposium on Personal, Indoor and Mobile Radio Communications, London, UK, 31 August–3 September 2020; pp. 1–6. [CrossRef]

58. Bertizzolo, L.; Polese, M.; Bonati, L.; Gosain, A.; Zorzi, M.; Melodia, T. MmBAC: Location-Aided MmWave Backhaul Management for UAV-Based Aerial Cells. In Proceedings of the 3rd ACM Workshop on Millimeter-Wave Networks and Sensing Systems, Los Cabos, Mexico, 25 October 2019; pp. 7–12. [CrossRef]

59. Polese, M.; Bertizzolo, L.; Bonati, L.; Gosain, A.; Melodia, T. An Experimental MmWave Channel Model for UAV-to-UAV Communications. In Proceedings of the 4th ACM Workshop on Millimeter-Wave Networks and Sensing Systems, London, UK, 25 September 2020. [CrossRef]

60. Yan, H.; Domae, B.W.; Cabric, D. MmRAPID: Machine Learning Assisted Noncoherent Compressive Millimeter-Wave Beam Alignment. In Proceedings of the 4th ACM Workshop on Millimeter-Wave Networks and Sensing Systems, London, UK, 25 September 2020. [CrossRef]

61. De Beelde, B.; Lopéz, A.A.; Plets, D.; Yusuf, M.; Tanghe, E.; Joseph, W. Directive mmWave radio channel modeling in a ship hull. *Int. J. Microw. Wirel. Technol.* **2021**, 1–12. [CrossRef]

62. Langen, B.; Lober, G.; Herzig, W. Reflection and transmission behaviour of building materials at 60 GHz. In Proceedings of the 5th IEEE International Symposium on Personal, Indoor and Mobile Radio Communications, Wireless Networks-Catching the Mobile Future, The Hague, The Netherlands, 18–23 September 1994; Volume 2, pp. 505–509. [CrossRef]

63. Jacob, M.; Priebe, S.; Maltsev, A.; Lomayev, A.; Erceg, V.; Kurner, T. A ray tracing based stochastic human blockage model for the IEEE 802.11ad 60 GHz channel model. In Proceedings of the 5th European Conference on Antennas and Propagation (EUCAP), Rome, Italy, 11–15 April 2011; pp. 3084–3088.